Chemical
Science

ROYAL SOCIETY
OF CHEMISTRY

EDGE ARTICLE

View Article Online
View Journal | View Issue

Check for updates

Cite this: *Chem. Sci.*, 2025, **16**, 5275

All publication charges for this article have been paid for by the Royal Society of Chemistry

Single-molecule-level detection of interfacial molecular structures and ultrafast dynamics†

Xiaoxuan Zheng,[ab] Junjun Tan,*[b] Quanbing Pei,[a] Yi Luo*[ab] and Shuji Ye*[ab]

Received 20th November 2024
Accepted 15th February 2025

DOI: 10.1039/d4sc07863b

rsc.li/chemical-science

Elucidating the ultrafast dynamics of interfacial molecules at the single-molecule level is pivotal for advancing our understanding of fundamental chemical and biological processes. Here, for the first time, we realized detection of ultrafast vibrational dynamics by a novel technique that integrates femtosecond sum frequency generation vibrational spectroscopy (SFG-VS) with nanoparticle-on-mirror (NPoM) nanocavities (NPoM-SFG-VS). Using a symmetric stretching vibrational mode of *para*-nitrothiophenol (ν_{NO_2}) as a probe, we have successfully identified signals from self-assembled monolayers (SAMs) comprising ~60 molecules, demonstrating the single-molecule-level sensitivity of the NPoM-SFG-VS. The dephasing time and vibrational relaxation time of ν_{NO_2} at the single-molecule level were determined to be 0.33 ± 0.01 ps and 2.2 ± 0.2 ps, respectively. By controlling the solution concentration used to prepare SAMs (C), a correlation between peak frequency of ν_{NO_2} and C is established. It was found that single-molecule-level detection was achieved at $C \leq 10^{-10}$ M. With this protocol, microregion distribution of interfacial molecule number can be mapped using NPoM-SFG imaging. This work provides insights into the structures and vibrational dynamics of individual interfacial molecules, aiding in precise engineering of surface properties and reactivity.

Introduction

Dynamics of individual molecules on ultrafast timescales plays a prominent role in chemistry, physics, molecular biology, quantum optics, and superresolution microscopy.[1–3] It requires developing a cutting-edge technique that can provide structural and dynamical details with femtosecond temporal resolution and allow for ultrasensitive detection of molecules at single-molecule level. It has been shown that surface-enhanced vibrational spectroscopy (SEVS) such as infrared absorption (SEIRA) and Raman scattering (SERS) can largely enhance the molecular vibrational signals through amplifying the electromagnetic fields generated by the excitation of localized metal plasmons.[4–10] In particular, the molecular detection sensitivity can be further improved by using the nanoparticle-on-mirror (NPoM) method. The highly localized and concentrated light in subnanoscale volumes enables the generation of strong light-matter coupling, pushing the structural detection into the single-molecule level.[11–16] Spatial confinement at the nanoscale plays a pivotal role in numerous fields, such as biology,[17,18] materials science,[19,20] and photonics.[21–24] For instance, the confinement of light within the nanoscale space is fundamental to the development of nanophotonics, which is crucial for applications including high-resolution imaging, sensitive sensing, and precise manipulation of chemical reactions.[21–24] In the realm of materials science, the investigation of the "nano-confinement effect" holds substantial significance. Materials with nanoconfinement exhibit unexpected physical and chemical properties,[25,26] which significantly influence their reactivity and performance.

On the other hand, femtosecond time-resolved sum frequency generation vibrational spectroscopy (SFG-VS) is a coherent femtosecond second-order nonlinear spectroscopy technique that permits elucidation of the structure and ultrafast dynamics of interfacial molecules.[27–31] Therefore, it is anticipated that the integration of femtosecond SFG-VS with nanocavities fabricated from NPoM (NPoM-SFG-VS) (Fig. 1) may provide a possible avenue to probe the dynamics of individual interfacial molecules on an ultrafast timescale. To materialize this idea, we used 4-nitrothiophenol (NTP) in plasmonic nanocavities as the model and examined the detection limit of NPoM-SFG-VS by determining the spectral and dynamical features of the symmetric stretching vibrational mode of the nitro group (ν_{NO_2}) of NTP across a range of molecule numbers. It should be clarified that the SFG selection rule may be disrupted as the electric dipole approximation is no longer valid due to the strong localized optical fields generated in the near field, which are spatially non-uniform or have significant gradients.[32,33] To minimize this effect, we prepared the samples in monolayer so

---

[a] Hefei National Research Center for Physical Sciences at the Microscale, Department of Chemical Physics, University of Science and Technology of China, Hefei, Anhui, 230026, China. E-mail: shujiye@ustc.edu.cn; yiluo@ustc.edu.cn

[b] Hefei National Laboratory, University of Science and Technology of China, Hefei, Anhui, 230088, China. E-mail: jjtan@ustc.edu.cn

† Electronic supplementary information (ESI) available. See DOI: https://doi.org/10.1039/d4sc07863b

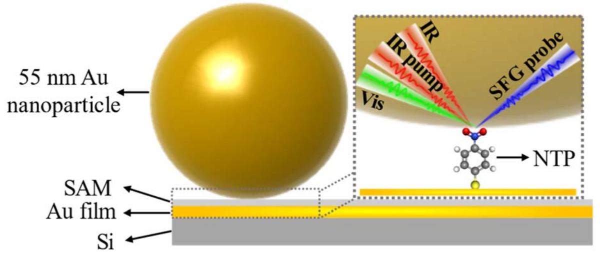

Fig. 1 Scheme for the integration of femtosecond time-resolved SFG-VS with nanocavity fabricated from NPoM (NPoM-SFG-VS). SAM: self-assembled monolayer. NTP: 4-nitrothiophenol. All the SFG measurements were carried out in the air, rather than in solutions. Note that the figure is only a schematic diagram, the Au film may contain short terraces and atomic steps, and the NTP has a special tilt angle on Au film.

that the signal originates solely from the interfacial monolayer. The nitro group was chosen because it has high reactivity and significant cross-sections for infrared absorption and Raman scattering and has served as an exemplary model for studying plasmon-mediated chemical reactions (PMCRs).[34–40] An increase in the number of NTP molecules leads to a blueshift in the peak frequency of ν_{NO_2}, a slow dephasing time and a fast vibrational relaxation time. NPoM-SFG-VS can detect the structure and ultrafast vibrational dynamics of samples composed of only ∼60 molecules. The dephasing time and vibrational relaxation time of single-molecule-level ν_{NO_2} were determined to be 0.33 ± 0.01 ps and 2.2 ± 0.2 ps, respectively. To the best of our knowledge, this is the first experimental observation of ultrafast vibrational dynamics at the single-molecule level. This work confirms the feasibility of probing the ultrafast dynamics of individual molecules by NPoM-SFG-VS. Furthermore, the combination of NPoM and sum frequency generation vibrational imaging (SFG-VI) (NPoM-SFG-VI) can be used to determine the distribution of microzone molecular density by measuring the peak frequency of the ν_{NO_2} mode.[41–43] These findings will aid in deepening our understanding of single-molecule behavior and advancing the field of single-molecule reaction dynamics.

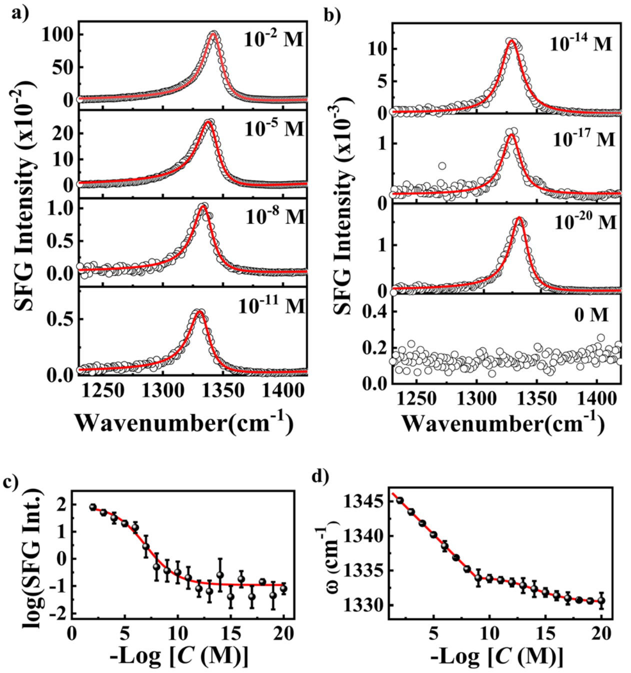

Fig. 2 (a and b) ppp SFG spectra of different concentrations of NTP in the NO_2 stretching region. (c) The log(SFG intensity) and (d) ω values of samples self-assembled by a range of concentrations of NTP solutions are plotted against concentration. 10^{-2}, 10^{-5}, 10^{-8}, 10^{-11}, 10^{-14}, 10^{-17}, 10^{-20}, 0 M and the symbol "*C*" represent the concentration of the solution that was used to prepare the SAMs.

Results and discussion

Single-molecule-level detection of interfacial molecular structures

We first investigated the SFG spectra of ν_{NO_2} in the nanocavities using NPoM-SFG-VS (Fig. 1). NPoM-SFG-VS setup adopts a geometry in a noncollinear configuration (details are given in ESI†). The NPoM samples were constructed by depositing Au nanoparticles with a diameter of ∼55 nm on a smooth Au film on which the target molecules with various molecular numbers were initially self-assembled to form self-assembled monolayers (SAMs). The procedure details are given in the ESI.† Fig. 2a and b display the typical ppp SFG spectra of the NPoM samples prepared with a 10 mL NTP solution of concentrations (C) ranging from 10^{-2} to 10^{-20} M. It needs mention that the symbol "C" shown in the figures and appeared in the main text and ESI† refers to the concentration of the solution that was used to prepare the SAMs, and it does not mean that the experiments were performed in that solution. The ppp SFG spectra ranging from 1100 cm^{-1} to 1800 cm^{-1} for all concentrations are presented in Fig. S4.† The spectra were dominated by a distinct peak at ∼1340 cm^{-1} with a peak width of 9 ± 2 cm^{-1}. This peak is attributed to the symmetric stretching vibrational mode of the nitro group (ν_{NO_2}).[37,40] The narrow bandwidth indicated the absence of vibrational ladder climbing.[44] It is evident that NPoM-SFG-VS can probe the signals from self-assembled samples prepared with 10 mL of 10^{-20} M NTP solution, corresponding to ∼60 molecules. In contrast, in the absence of the nanocavity structure, the detection sensitivity reached only 10^{-8} M (Fig. S6†). This enhanced sensitivity is ascribed to the strong signal enhancement obtained from the strong localized light field of the nanocavity. Fig. 2a and b show a discernible attenuation in peak intensity with decreasing concentration. Fig. 2c shows the dependence of the SFG intensity on C. The intensity in Fig. 2c refers to the maximal intensity rather than the average intensity of a particular concentration of samples in the experiment. Theoretically, the coverage of samples prepared at high concentrations, such as 10^{-5} M and 10^{-2} M could be identical over an infinite time period. However, the number of self-assembled molecules in a limited assembly time is actually affected by the concentration of the bulk solutions, leading to concentration-dependent coverage. The signal is weak and random when $C \leq 10^{-10}$ M. Note that as C decreases, the sample signal cannot be detected on the whole gold film and the probability of the signal is obviously decreasing,[45] which requires a deliberate search for the spot. Notably, signal detection is more readily achieved at the periphery of the gold film rather than at the center.[46] When $C \leq 10^{-10}$ M, there is no enrichment effect of probe molecules in the laser focusing region, which is a feature of the single-molecule level, indicating that the number of detectable molecules reaches the level of a single or a few molecules. This observation is corroborated by recent SERS studies, which have identified single-molecule-level detection at concentrations below 10^{-10} M or 10^{-11} M.[47,48] Despite the similar signal intensity when $C \leq 10^{-10}$ M, the probability of detecting a signal is greatly reduced as the concentration decreases.[45] The most absence of signals at low concentrations and lack of signal peaks from other species (see the case of 0 M at Fig. 2b) can rule out the influence of other materials on the experimental results. The peak frequency (ω) of ν_{NO_2} redshifted as C decreases. In theory, the peak frequency of a vibrational mode is related to intermolecular coupling, which manifests as the delocalization of electronic or vibrational wavefunctions.[49,50] As the concentration decreases, the intermolecular coupling becomes weak, leading to a redshift in the peak frequency. To qualitatively analyze the concentration-dependent change in the frequency, we fitted the spectra using eqn (S1).† The typical fitting parameters are listed in Table S1.† The ω values are 1345.1 ± 0.4, 1343.5 ± 0.4, 1341.8 ± 0.3, 1340.2 ± 0.3, 1338.5 ± 0.7, 1336.9 ± 0.2, 1335.2 ± 0.4, 1333.9 ± 1.2, 1333.8 ± 0.5, 1333.6 ± 0.4, 1333.3 ± 0.6, 1332.8 ± 1.1, 1332.3 ± 1.2, 1331.8 ± 0.6, 1331.4 ± 0.7, 1331.0 ± 0.9, 1330.7 ± 0.1, 1330.6 ± 0.4, and 1330.6 ± 1.1 cm^{-1} for C from 10^{-2} to 10^{-20} M, respectively. The error bars indicate the results of more than 5 different separately prepared samples. Fig. 2d shows the concentration dependence of the frequency. A linear correlation between ω and C ($\omega = 1348.3 + 1.6\log[\text{C}]$) is observed at $C > 10^{-10}$ M. However, ω at $C \leq 10^{-10}$ M displays a subtle downward trajectory as the concentration decreases, further illustrating that the samples exhibit single-molecule-level features at $C \leq 10^{-10}$ M and that significant aggregation begins to occur only when the concentration increases to greater than 10^{-10} M.

Single-molecule-level detection of vibrational dynamics

We turned to investigate ultrafast dephasing and vibrational relaxation dynamics of ν_{NO_2}. The dephasing dynamics can be probed by SFG free induction decay (SFG-FID) measurements which has been demonstrated to be an effective method for gauging the interaction between a chemical group and its environment (a scheme for SFG-FID spectroscopy is shown in Fig. S2c†).[29,51–53] Fig. 3a illustrates the dephasing dynamics at several typical concentrations. More comprehensive spectra are detailed in Fig. S9.† The absence of oscillatory features in the SFG-FID spectra confirms the noninterference of ν_{NO_2} with other vibrational modes within the probed region, signifying that the spectra solely represent the ν_{NO_2}-environment interaction. The SFG-FID curves were fitted to acquire information on the dephasing time (τ_{FID}) by the procedure outlined in earlier studies, and the fitting equations are presented in the ESI.†[29,54]

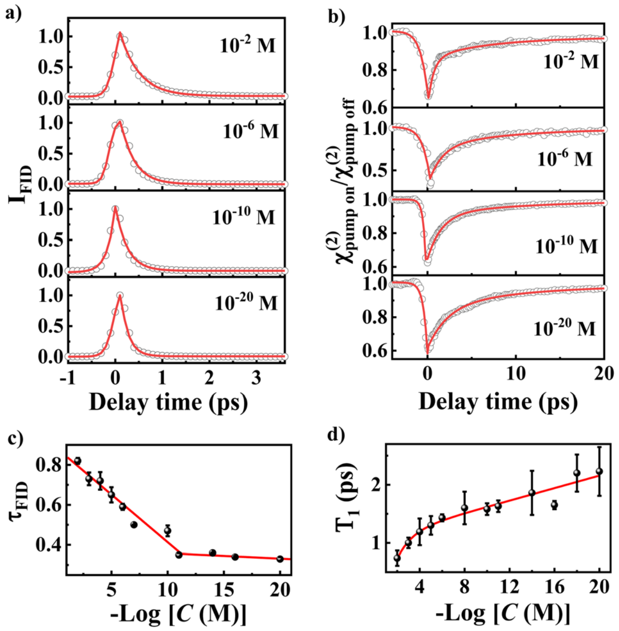

Fig. 3 (a) SFG-FID spectra and (b) ppp $\chi^{(2)}$ decay of ν_{NO_2} for $C = 10^{-2}$, 10^{-6}, 10^{-10}, and 10^{-20} M. (c) τ_{FID} and (d) T_1 are plotted against C. 10^{-2}, 10^{-6}, 10^{-10}, 10^{-20} M, and the symbol "C" represent the concentration of the solution that was used to prepare the SAMs.

Fig. 3c reveals a diminution in τ_{FID} with decreasing C, with τ_{FID} values of 0.82 ± 0.02 ps and 0.33 ± 0.01 ps corresponding to 10^{-2} M and 10^{-20} M, respectively. τ_{FID} serves as an index of the coupling strength between a molecule and its environment, and is modulated by factors such as the phonon modes of substrates, surface ligands, and solvent interactions.[55] Earlier study indicated that the influence of the concentrations on the orientation of the SAM with an immersion time of 12 h is quite small.[56] The contribution of orientation to the coupling between molecule and substrate should be negligible. Herein, the main cause is the coupling between ν_{NO_2} and the metal substrate phonon.[57–59] It has been indicated that the molecular adsorbates on metal surfaces dissipate energy through the energy exchange with substrate phonons.[57–59] As a result, more substrate phonons participate in the energy dissipation of each ν_{NO_2} mode as the interfacial density of NTP molecules decreases.

Fig. 3b shows the effective SFG strength ($\chi^{(2)}$) decay of ν_{NO_2} for typical concentration. Vibrational relaxation dynamics comprise information on the potential energy surface and relaxation dynamics along the chemical reaction pathway, which is essential for the microscopic understanding of interfacial molecular processes, especially surface reactions (a scheme for broadband IR pump/SFG-probe spectroscopy is shown in Fig. S2d†).[60–65] Because SFG detects the interfacial population number of a vibrational ground state (ν_0), excitation of ν_{NO_2} from ν_0 to the first vibrational excited state (ν_1) reduces the SFG intensity.[30,66] Due to the nanocavity-enhanced vibrational excitation proportion of ν_{NO_2}, we can observe clear bleaching, as shown in Fig. 3b.[67,68] After bleaching, the relaxation of the ν_1 state to the intermediate state leads to a gradual recovery of the intensity. The ultrafast vibrational dynamics of

ν_{NO_2} exhibit biexponential decays with a high percentage of a fast component (T_1) and a small percentage of a slow component (T_2). T_1 arises from the population transfer among different modes, while T_2 is mainly attributed to the intramolecular vibrational relaxation in combination with a nonadiabatic relaxation originating from the excitation of electron–hole pairs (EHPs) in the Au substrate and Au nanoparticles.[69,70] As detailed in Table S3,† T_2 remains relatively invariant at approximately 10 ± 2 ps, indicating consistent coupling between the molecules and EHPs. However, T_1 exhibits significant variation with C. T_1 is 0.7 ± 0.1, 1.0 ± 0.1, 1.2 ± 0.2, 1.3 ± 0.2, 1.4 ± 0.1, 1.6 ± 0.3, 1.6 ± 0.1, 1.6 ± 0.1, 1.9 ± 0.4, 1.7 ± 0.1, 2.2 ± 0.3 and 2.2 ± 0.4 ps for $C = 10^{-2}$, 10^{-3}, 10^{-4}, 10^{-5}, 10^{-6}, 10^{-8}, 10^{-10}, 10^{-11}, 10^{-14}, 10^{-16}, 10^{-18} and 10^{-20} M, respectively. The increase in T_1 is attributed to the reduced efficiency of intermode energy dissipation because the strength of intermolecular decoupling increases as the concentration decreases. A recent report indicated that molecular decoupling is the initial step of a chemical reaction and the likelihood of a reaction escalating with increasing intermolecular decoupling.[71] Therefore, a longer T_1 signifies an elevated probability of chemical reaction.[72]

Further evidence for single-molecule-level detection

With the NPoM-SFG-VS protocol, the vibrational frequency (ω), dephasing time (τ_{FID}) and vibrational relaxation time (T_1) of ν_{NO_2} at the single-molecule level were determined to be 1330.6 ± 1.1 cm^{-1}, 0.33 ± 0.01 ps, and 2.2 ± 0.2 ps for ν_{NO_2}, respectively. These results can be further verified by mixing NTP and *p*-mercaptobenzonitrile (MBN). The nitro percentage (R_{NTP}) was controlled by preparing mixed SAMs ($C = 10^{-2}$ M) using ethanol solutions of NTP and MBN with molar ratios (m) ranging from 10 : 0 (100% NTP) to 0 : 10 (0% NTP) ($R_{NTP} = m_{NTP}/(m_{NTP} + m_{MBN})$). Mixing of different thiol molecules is a common procedure to change the degree of coupling of the target molecule.[49,71] Mixing of NTP and MBN has been used to obtain the single-molecule-level NTP behavior. SERS and X-ray photoelectron spectroscopy (XPS) results have verified that the NTP/MBN mixture is relatively homogeneous and no phase separation was observed.[71] The SFG spectra in the 1250–1700 cm^{-1} range (Fig. S11†) display three distinct peaks at 1335–1346 cm^{-1}, ~1570 cm^{-1} and ~1582 cm^{-1}, which are attributed to ν_{NO_2}, the aromatic C=C stretching mode of NTP ($\nu_{C=C,\ NTP}$), and the aromatic C=C stretching mode of MBN ($\nu_{C=C,\ MBN}$), respectively.[49,71] The proportional change in SFG intensity of the $\nu_{C=C,\ NTP}$ and $\nu_{C=C,\ MBN}$ modes illustrates the effectiveness of the dilution strategy. Fig. 4a–c show the ppp SFG spectra in the NO$_2$ stretching region, SFG-FID spectra of ν_{NO_2}, and ppp $\chi^{(2)}$ decay of ν_{NO_2}. Using the same procedure, we determined the values of ω, τ_{FID}, and T_1 of ν_{NO_2}. The results are given in Table 1 and Fig. 4d–f. It is evident that the values of ω, τ_{FID}, and T_1 all vary significantly with the R_{NTP}. Strong linear correlations between the values and R_{NTP} were observed. Linear fitting for these correlations in Fig. 4d–f yields an extrapolated value of $\omega = 1333.5$ cm^{-1}, $\tau_{FID} = 0.33$ ps, and $T_1 = 2.3$ ps at $R_{NTP} = 0$. These values are in good agreement with those determined using ultralow concentrations, further validating the structure and dynamics measurements at the single-molecule level. These findings underscore the efficacy of our approach in capturing the structural and dynamical properties of molecules at interfaces with single-molecule-level resolution.

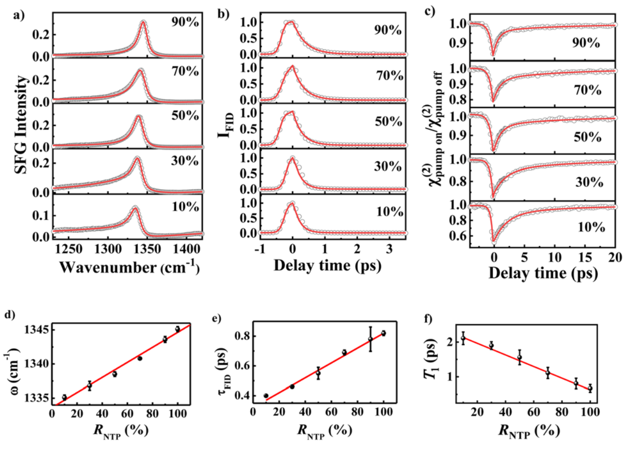

Fig. 4 (a) The ppp SFG spectra in the NO$_2$ stretching region. (b) SFG-FID spectra of ν_{NO_2}. (c) The ppp $\chi^{(2)}$ decay of ν_{NO_2}. (d) The ω, (e) τ_{FID}, and (f) T_1 are plotted against R_{NTP}.

Single-molecule-level detection of microzone using NPoM-SFG-VI

Fig. 2d and 4d indicate that the peak frequency is strongly related to the local concentration. Therefore, the peak shifts can serve as spectroscopic indicators of the microzone molecular density. The peak shifts have been used for microscopic "imaging" and to measure disorder and distance between molecules.[49,50,73] Here, we employed NPoM-SFG-VI to visualize the distribution of interfacial microzone concentrations (C_M). NPoM-SFG-VI setup uses a geometry in a collinear configuration (Fig. S3†). A total of 1681 spectra were collected in a space of 120 µm × 120 µm with a space resolution of 3 µm. The spectra were then fitted using eqn (S1)† to extract the microzone frequency (ω_M) and microzone peak strength ($\chi_M^{(2)}$). The image was then constructed using the values of ω_M and C_M. C_M is estimated

Table 1 The values of ω, τ_{FID}, and T_1 vary with the R_{NTP}

R_{NTP}	100%	90%	70%	50%	30%	10%
ω (cm^{-1})	1345.1 ± 0.4	1343.6 ± 0.4	1340.8 ± 0.1	1338.5 ± 0.3	1336.8 ± 0.6	1335.1 ± 0.4
τ_{FID} (ps)	0.82 ± 0.02	0.78 ± 0.08	0.69 ± 0.02	0.55 ± 0.04	0.46 ± 0.01	0.40 ± 0.01
T_1 (ps)	0.7 ± 0.1	0.8 ± 0.2	1.1 ± 0.2	1.6 ± 0.2	1.9 ± 0.1	2.1 ± 0.2

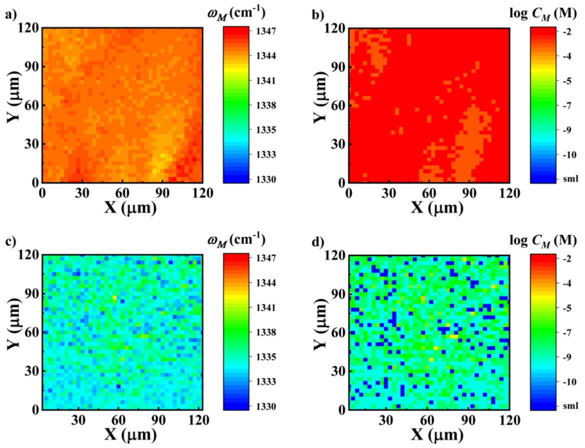

Fig. 5 Images constructed with the ν_{NO_2} frequency (a and c) and its corresponding surface microzone concentration (C_M) (b and d). (a) and (b) Sample prepared with $C = 10^{-2}$ M; (c) and (d) sample prepared with $C = 10^{-8}$ M. The symbol "C" represents the concentration of the solution that was used to prepare the SAMs. sml: single-molecule level.

using the relationship $\left(\log[C_M] = \mathrm{round}\left[\frac{\omega_M - 1348.3}{1.6}\right]\right)$ determined by Fig. 2d with $C > 10^{-10}$ M. Here, round refers to the rounding function. Fig. 5 shows the microzone frequency and surface microzone concentration for the $C = 10^{-2}$ and 10^{-8} M samples. The 10^{-2} M sample exhibits a relatively uniform C_M distribution because the entire gold film is almost completely covered with molecules. In contrast, for the 10^{-8} M sample, some areas had C_M higher than 10^{-8} M, while some areas had C_M of $\leq 10^{-10}$ M, with a peak frequency of $\leq$1333.2 cm^{-1}, indicating that the molecules in this area were distributed at the single-molecule level. Although the C_M distribution spans a wide range for the 10^{-8} M sample, the average ω for this sample is 1335.0 cm^{-1}, agreeing well with the results presented in Fig. 2d. Notably, the SFG intensity at different microregions depends on the hotspot strength and there is no definite correlation between the local microzone concentration and the SFG intensity. Therefore, mapping using SFG intensity did not allow us to discern the distribution of the interfacial microzone molecular density. NPoM-SFG-VI displays a strong ability to extract detailed spectroscopic information from microregions, aiding in analyzing microregion differences in spatially confined materials.

Conclusion

In this study, we have successfully demonstrated the ability to probe the structure and ultrafast dynamics of individual molecules at interfaces using NPoM-SFG-VS. By utilizing NTP in plasmonic nanocavities as a model system, we demonstrated the detection of structural and dynamical features from samples containing as few as ~60 molecules. We determined the dephasing time (τ_{FID}) and vibrational relaxation time (T_1) of ν_{NO_2} at the single-molecular level for the first time and elucidated the effect of intermolecular coupling on these dynamical properties. The τ_{FID} and T_1 of ν_{NO_2} at the single-molecule level were determined to be 0.33 ± 0.01 ps and 2.2 ± 0.2 ps, respectively. These findings provide unprecedented insights into single-molecule behavior and lay the foundation for advancing the field of single-molecule reaction dynamics. The developed techniques, NPoM-SFG-VS and NPoM-SFG-VI, hold immense potential for applications in chemistry, physics, molecular biology, and superresolution microscopy. In particular, NPoM-SFG-VI demonstrates a robust ability to obtain detailed spectroscopic information from microregions, even at ultralow concentrations. Visualization of microregion concentration distributions can provide valuable insights into the spatial heterogeneity of chemical reactions and the behavior of molecules at interfaces.

Methods

Materials and sample preparation

4-Nitrothiophenol (NTP, >95%) was purchased from Aladdin. 4-Mercaptobenzonitrile (MBN, >97%) was purchased from Shanghai Haohong Scientific Co., Ltd. *n*-hexane (≥99.7%) and ethanol (≥99.7%) were obtained from Sinopharm Chemical Reagent Co., Ltd. All of the chemicals were used as received. Ultrapure deionized (DI) water was purified by a Milli-Q purification system.

The samples were prepared by the following method: first, a clean smooth gold film (a 10 nm thick Cr layer was evaporated onto a rotating silicon wafer, followed by a 100 nm thick Au layer) was soaked in the target molecular solution (in ethanol) overnight to obtain a well-assembled SAM. NPoMs were made by dispersing gold nanoparticles (Au NPs) on Au-SAM. Au NPs were synthesized according to previous work.[74] The NP diameter was approximately 55 nm. Then, the target molecules were covered with a layer of closely packed AuNPs using the Langmuir–Blodgett (L–B) method.[75,76]

SFG-VS experiments

All the SFG experiments were all conducted utilizing a home-built time-resolved SFG-VS setup with a time resolution of 100 fs. The information about the detailed instrument parameters can be found in our previous publications.[30,31,77,78]

For the SFG-FID instrumentation,[29] it was required to remove the pulse shaper device for the 800 nm visible light in the frequency domain spectral measurement system and to change the visible light into femtosecond light as well. The area of the spectra obtained at each delay time is used as the signal intensity of the time-domain spectra, and the delay time corresponding to the highest point of the signal is set as the time zero point.

For the IR pump-SFG probe time-resolved SFG instrumentation, the pump-on and pump-off SFG signals were controlled by chopping the pump IR using an optical chopper and were split by a galvo mirror and imaged onto different rows of the CCD chip. According to the ratio of the processed pump-on and pump-off spectra for the corresponding delay time, the population information at a certain delay time is determined. The detailed procedures of fitting and data analysis have been described in our published studies.[30,79]

Data availability

The data that support the findings of this study are available from the corresponding author upon reasonable request.

Author contributions

S. J. Ye, and Y. Luo supervised the project. X. X. Zheng, and S. J. Ye designed the experiments. X. X. Zheng, Q. B. Pei, and J. J. Tan performed the experiments and analysed the data. X. X. Zheng, J. J. Tan, Y. Luo and S. J. Ye contributed to interpretation of the data. X. X. Zheng and S. J. Ye wrote the manuscript. All authors discussed the results of the study.

Conflicts of interest

The authors declare no competing financial interest.

Acknowledgements

This work was supported by the National Natural Science Foundation of China (21925302, 92250306, 22273094), the Innovation Program for Quantum Science and Technology (2021ZD0303303), and the Strategic Priority Research Program of the Chinese Academy of Sciences (XDB0450202).

References

1 N. L. Gruenke, M. F. Cardinal, M. O. McAnally, R. R. Frontiera, G. C. Schatz and R. P. Van Duyne, Ultrafast and Nonlinear Surface-Enhanced Raman Spectroscopy, *Chem. Soc. Rev.*, 2016, **45**, 2263–2290.

2 N. Alarcos, B. Cohen, M. Ziółek and A. Douhal, Photochemistry and Photophysics in Silica-Based Materials: Ultrafast and Single Molecule Spectroscopy Observation, *Chem. Rev.*, 2017, **117**, 13639–13720.

3 D. Brinks, R. Hildner, E. M. H. P. van Dijk, F. D. Stefani, J. B. Nieder, J. Hernando and N. F. van Hulst, Ultrafast Dynamics of Single Molecules, *Chem. Soc. Rev.*, 2014, **43**, 2476–2491.

4 J. M. Nam, J. W. Oh, H. Lee and Y. D. Suh, Plasmonic Nanogap-Enhanced Raman Scattering with Nanoparticles, *Acc. Chem. Res.*, 2016, **49**, 2746–2755.

5 B. Sharma, R. R. Frontiera, A. I. Henry, E. Ringe and R. P. Van Duyne, SERS: Materials, Applications, and the Future, *Mater. Today*, 2012, **15**, 16–25.

6 E. C. Le Ru and P. G. Etchegoin, Single-Molecule Surface-Enhanced Raman Spectroscopy, *Annu. Rev. Phys. Chem.*, 2012, **63**, 65–87.

7 T. Schmid, L. Opilik, C. Blum and R. Zenobi, Nanoscale Chemical Imaging Using Tip-Enhanced Raman Spectroscopy: A Critical Review, *Angew. Chem., Int. Ed.*, 2013, **52**, 5940–5954.

8 C. Zong, M. Xu, L. J. Xu, T. Wei, X. Ma, X. S. Zheng, R. Hu and B. Ren, Surface-Enhanced Raman Spectroscopy for Bioanalysis: Reliability and Challenges, *Chem. Rev.*, 2018, **118**, 4946–4980.

9 A. B. Zrimsek, N. Chiang, M. Mattei, S. Zaleski, M. O. McAnally, C. T. Chapman, A. I. Henry, G. C. Schatz and R. P. Van Duyne, Single-Molecule Chemistry with Surface- and Tip-Enhanced Raman Spectroscopy, *Chem. Rev.*, 2017, **117**, 7583–7613.

10 A. J. Wilson, D. Devasia and P. K. Jain, Nanoscale Optical Imaging in Chemistry, *Chem. Soc. Rev.*, 2020, **49**, 6087–6112.

11 E. Oksenberg, I. Shlesinger, A. Xomalis, A. Baldi, J. J. Baumberg, A. F. Koenderink and E. C. Garnett, Energy-Resolved Plasmonic Chemistry in Individual Nanoreactors, *Nat. Nanotechnol.*, 2021, **16**, 1378–1385.

12 F. Benz, M. K. Schmidt, A. Dreismann, R. Chikkaraddy, Y. Zhang, A. Demetriadou, C. Carnegie, H. Ohadi, B. de Nijs, R. Esteban, J. Aizpurua and J. J. Baumberg, Single-Molecule Optomechanics in "Picocavities", *Science*, 2016, **354**, 726–729.

13 J. J. Baumberg, J. Aizpurua, M. H. Mikkelsen and D. R. Smith, Extreme Nanophotonics from Ultrathin Metallic Gaps, *Nat. Mater.*, 2019, **18**, 668–678.

14 W. Peng, J. W. Zhou, M. L. Li, L. Sun, Y. J. Zhang and J. F. Li, Construction of Nanoparticle-on-Mirror Nanocavities and Their Applications in Plasmon-Enhanced Spectroscopy, *Chem. Sci.*, 2024, **15**, 2697–2711.

15 S. Hu, E. Elliott, A. Sánchez-Iglesias, J. Huang, C. Guo, Y. Hou, M. Kamp, E. S. A. Goerlitzer, K. Bedingfield, B. de Nijs, J. Peng, A. Demetriadou, L. M. Liz-Marzán and J. J. Baumberg, Full Control of Plasmonic Nanocavities Using Gold Decahedra-on-Mirror Constructs with Monodisperse Facets, *Adv. Sci.*, 2023, **10**, 2207178.

16 R. Chikkaraddy, A. Xomalis, L. A. Jakob and J. J. Baumberg, Mid-Infrared-Perturbed Molecular Vibrational Signatures in Plasmonic Nanocavities, *Light Sci. Appl.*, 2022, **11**, 19.

17 N. Jain and V. Vogel, Spatial Confinement Downsizes the Inflammatory Response of Macrophages, *Nat. Mater.*, 2018, **17**, 1134–1144.

18 L. Shang, F. Ye, M. Li and Y. Zhao, Spatial Confinement toward Creating Artificial Living Systems, *Chem. Soc. Rev.*, 2022, **51**, 4075–4093.

19 J. Wordsworth, T. M. Benedetti, S. V. Somerville, W. Schuhmann, R. D. Tilley and J. J. Gooding, The Influence of Nanoconfinement on Electrocatalysis, *Angew. Chem., Int. Ed.*, 2022, **61**, e202200755.

20 X. Ren, Q. Wang, Y. Pu, Q. Sun, W. Sun and L. Lu, Synergizing Spatial Confinement and Dual-Metal Catalysis to Boost Sulfur Kinetics in Lithium-Sulfur Batteries, *Adv. Mater.*, 2023, **35**, 2304120.

21 R. Lemasters, M. Manjare, R. Freeman, F. Wang, L. G. Pierce, G. Hua, S. Urazhdin and H. Harutyunyan, Non-Thermal Emission in Gap-Mode Plasmon Photoluminescence, *Nat. Commun.*, 2024, **15**, 4468.

22 Y. U. Lee, G. B. M. Wisna, S. W. Hsu, J. Zhao, M. Lei, S. Li, A. R. Tao and Z. Liu, Imaging of Nanoscale Light

Confinement in Plasmonic Nanoantennas by Brownian Optical Microscopy, *ACS Nano*, 2020, **14**, 7666–7672.

23 H. Herzig Sheinfux, L. Orsini, M. Jung, I. Torre, M. Ceccanti, S. Marconi, R. Maniyara, D. Barcons Ruiz, A. Hötger, R. Bertini, S. Castilla, N. C. H. Hesp, E. Janzen, A. Holleitner, V. Pruneri, J. H. Edgar, G. Shvets and F. H. L. Koppens, High-Quality Nanocavities through Multimodal Confinement of Hyperbolic Polaritons in Hexagonal Boron Nitride, *Nat. Mater.*, 2024, **23**, 499–505.

24 V. Mkhitaryan, A. P. Weber, S. Abdullah, L. Fernández, Z. M. Abd El-Fattah, I. Piquero-Zulaica, H. Agarwal, K. García Díez, F. Schiller, J. E. Ortega and F. J. García de Abajo, Ultraconfined Plasmons in Atomically Thin Crystalline Silver Nanostructures, *Adv. Mater.*, 2024, **36**, 2302520.

25 L. Cai, J. Yang, Y. Lai, Y. Liang, R. Zhang, C. Gu, S. Kitagawa and P. Yin, Dynamics and Proton Conduction of Heterogeneously Confined Imidazole in Porous Coordination Polymers, *Angew. Chem., Int. Ed.*, 2023, **62**, e202211741.

26 S. Boyd, K. Ganeshan, W. Y. Tsai, T. Wu, S. Saeed, D. e. Jiang, N. Balke, A. C. T. van Duin and V. Augustyn, Effects of Interlayer Confinement and Hydration on Capacitive Charge Storage in Birnessite, *Nat. Mater.*, 2021, **20**, 1689–1694.

27 S. Nihonyanagi, A. Eftekhari-Bafrooei and E. Borguet, Ultrafast Vibrational Dynamics and Spectroscopy of a Siloxane Self-Assembled Monolayer, *J. Chem. Phys.*, 2011, **134**, 084701.

28 H. S. AlSalem and S. P. K. Koehler, Ultrafast Vibrational Dephasing Times of Modified Graphene, *J. Phys. Chem. C*, 2022, **126**, 7571–7575.

29 J. H. Zhang, R. Q. Pei, J. J. Tan, Z. J. Ni, S. J. Ye and Y. Luo, Visualizing Water Monomers and Chiral $OH^-(H_2O)$ Complexes Infiltrated in a Macroscopic Hydrophobic Teflon Matrix, *J. Am. Chem. Soc.*, 2023, **145**, 26925–26931.

30 J. J. Tan, B. X. Zhang, Y. Luo and S. J. Ye, Ultrafast Vibrational Dynamics of Membrane-Bound Peptides at the Lipid Bilayer/Water Interface, *Angew. Chem., Int. Ed.*, 2017, **56**, 12977–12981.

31 J. J. Tan, J. H. Zhang, C. Z. Li, Y. Luo and S. J. Ye, Ultrafast Energy Relaxation Dynamics of Amide I Vibrations Coupled with Protein-Bound Water Molecules, *Nat. Commun.*, 2019, **10**, 1010.

32 M. Yamaguchi and K. Nobusada, Large Hyperpolarizabilities of the Second Harmonic Generation Induced by Nonuniform Optical Near Fields, *J. Phys. Chem. C*, 2016, **120**, 23748–23755.

33 E. Poliani, M. R. Wagner, A. Vierck, F. Herziger, C. Nenstiel, F. Gannott, M. Schweiger, S. Fritze, A. Dadgar, J. Zaumseil, A. Krost, A. Hoffmann and J. Maultzsch, Breakdown of Far-Field Raman Selection Rules by Light-Plasmon Coupling Demonstrated by Tip-Enhanced Raman Scattering, *J. Phys. Chem. Lett.*, 2017, **8**, 5462–5471.

34 A. B. C. Mantilla, C. F. Wang, A. Krayev, Y. Gu, Z. D. Schultz and P. Z. El-Khoury, Classical vs. Quantum Plasmon-Induced Molecular Transformations at Metallic Nanojunctions, *Proc. Natl. Acad. Sci. U.S.A.*, 2024, **121**, e2319233121.

35 R. Wang, J. Li, J. Rigor, N. Large, P. Z. El-Khoury, A. Y. Rogachev and D. Kurouski, Direct Experimental Evidence of Hot Carrier-Driven Chemical Processes in Tip-Enhanced Raman Spectroscopy (TERS), *J. Phys. Chem. C*, 2020, **124**, 2238–2244.

36 H. K. Choi, K. S. Lee, H. H. Shin and Z. H. Kim, Identification of the First Elementary Step in the Photocatalytic Reduction of Nitrobenzenethiols on a Metallic Surface, *J. Phys. Chem. Lett.*, 2016, **7**, 4099–4104.

37 E. L. Keller and R. R. Frontiera, Ultrafast Nanoscale Raman Thermometry Proves Heating Is Not a Primary Mechanism for Plasmon-Driven Photocatalysis, *ACS Nano*, 2018, **12**, 5848–5855.

38 J. Zhang, S. A. Winget, Y. Wu, D. Su, X. Sun, Z. X. Xie and D. Qin, Ag@Au Concave Cuboctahedra: A Unique Probe for Monitoring Au-Catalyzed Reduction and Oxidation Reactions by Surface-Enhanced Raman Spectroscopy, *ACS Nano*, 2016, **10**, 2607–2616.

39 W. Xie and S. Schlücker, Hot Electron-Induced Reduction of Small Molecules on Photorecycling Metal Surfaces, *Nat. Commun.*, 2015, **6**, 7570.

40 Z. F. Cai, J. P. Merino, W. Fang, N. Kumar, J. O. Richardson, S. De Feyter and R. Zenobi, Molecular-Level Insights on Reactive Arrangement in On-Surface Photocatalytic Coupling Reactions Using Tip-Enhanced Raman Spectroscopy, *J. Am. Chem. Soc.*, 2022, **144**, 538–546.

41 S. A. Shah and S. Baldelli, Chemical Imaging of Surfaces with Sum Frequency Generation Vibrational Spectroscopy, *Acc. Chem. Res.*, 2020, **53**, 1139–1150.

42 K. Cimatu and S. Baldelli, Chemical Imaging of Corrosion: Sum Frequency Generation Imaging Microscopy of Cyanide on Gold at the Solid-Liquid Interface, *J. Am. Chem. Soc.*, 2008, **130**, 8030–8037.

43 V. Raghunathan, Y. Han, O. Korth, N. H. Ge and E. O. Potma, Rapid Vibrational Imaging with Sum Frequency Generation Microscopy, *Opt. Lett.*, 2011, **36**, 3891–3893.

44 H. H. Shin, J. Jeong, Y. Nam, K. S. Lee, G. J. Yeon, H. Lee, S. Y. Lee, S. Park, H. Park, J. Y. Lee and Z. H. Kim, Vibrationally Hot Reactants in a Plasmon-Assisted Chemical Reaction, *J. Am. Chem. Soc.*, 2023, **145**, 12264–12274.

45 H. Zhang, L. Yang, M. Zhang, H. Wei, L. Tong, H. Xu and Z. Li, A Statistical Route to Robust SERS Quantitation Beyond the Single-Molecule Level, *Nano Lett.*, 2024, **24**, 11116–11123.

46 J. M. Marr and Z. D. Schultz, Imaging Electric Fields in SERS and TERS Using the Vibrational Stark Effect, *J. Phys. Chem. Lett.*, 2013, **4**, 3268–3272.

47 C. Lin, S. Liang, Y. Peng, L. Long, Y. Li, Z. Huang, N. V. Long, X. Luo, J. Liu, Z. Li and Y. Yang, Visualized SERS Imaging of Single Molecule by Ag/Black Phosphorus Nanosheets, *Nano-Micro Lett.*, 2022, **14**, 75.

48 H. Yang, H. Mo, J. Zhang, L. Hong and Z. Y. Li, Observation of Single-Molecule Raman Spectroscopy Enabled by Synergic Electromagnetic and Chemical Enhancement, *Photon X*, 2024, **5**, 3.

49 T. P. Gray, J. Nishida, S. C. Johnson and M. B. Raschke, 2D Vibrational Exciton Nanoimaging of Domain Formation in Self-Assembled Monolayers, *Nano Lett.*, 2021, **21**, 5754–5759.

50 E. A. Muller, T. P. Gray, Z. Zhou, X. Cheng, O. Khatib, H. A. Bechtel and M. B. Raschke, Vibrational Exciton Nanoimaging of Phases and Domains in Porphyrin Nanocrystals, *Proc. Natl. Acad. Sci. U.S.A.*, 2020, **117**, 7030–7037.

51 A. Boulesbaa and E. Borguet, Vibrational Dynamics of Interfacial Water by Free Induction Decay Sum Frequency Generation (FID-SFG) at the $Al_2O_3(1120)/H_2O$ Interface, *J. Phys. Chem. Lett.*, 2014, **5**, 528–533.

52 A. Boulesbaa and E. Borguet, Capturing the Ultrafast Vibrational Decoherence of Hydrogen Bonding in Interfacial Water, *J. Phys. Chem. Lett.*, 2016, **7**, 5080–5085.

53 P. Hu, X. Li, B. Li, X. Han, F. Zhang, K. C. Chou, Z. Chen and X. Lu, Molecular Coupling between Organic Molecules and Metal, *J. Phys. Chem. Lett.*, 2018, **9**, 5167–5172.

54 A. Eftekhari-Bafrooei, S. Nihonyanagi and E. Borguet, Spectroscopy and Dynamics of the Multiple Free OH Species at an Aqueous/Hydrophobic Interface, *J. Phys. Chem. C*, 2012, **116**, 21734–21741.

55 Y. He, G. Chen, M. Xu, Y. Liu and Z. Wang, Vibrational Dephasing of Self-Assembling Monolayer on Gold Surface, *J. Lumin.*, 2014, **152**, 244–246.

56 R. H. Terrill, T. A. Tanzer and P. W. Bohn, Structural Evolution of Hexadecanethiol Monolayers on Gold during Assembly: Substrate and Concentration Dependence of Monolayer Structure and Crystallinity, *Langmuir*, 1998, **14**, 845–854.

57 C. Yi, P. D. Dongare, M. N. Su, W. Wang, D. Chakraborty, F. Wen, W. S. Chang, J. E. Sader, P. Nordlander, N. J. Halas and S. Link, Vibrational Coupling in Plasmonic Molecules, *Proc. Natl. Acad. Sci. U.S.A.*, 2017, **114**, 11621–11626.

58 R. J. Maurer, M. Askerka, V. S. Batista and J. C. Tully, Ab Initio Tensorial Electronic Friction for Molecules on Metal Surfaces: Nonadiabatic Vibrational Relaxation, *Phys. Rev. B*, 2016, **94**, 115432.

59 S. P. Rittmeyer, V. J. Bukas and K. Reuter, Energy Dissipation at Metal Surfaces, *Adv. Phys. X*, 2018, **3**, 1381574.

60 J. C. Owrutsky, D. Raftery and R. M. Hochstrasser, Vibrational Relaxation Dynamics in Solutions, *Annu. Rev. Phys. Chem.*, 1994, **45**, 519–555.

61 F. F. Crim, Chemical Dynamics of Vibrationally Excited Molecules: Controlling Reactions in Gases and on Surfaces, *Proc. Natl. Acad. Sci. U.S.A.*, 2008, **105**, 12654–12661.

62 J. F. Cahoon, K. R. Sawyer, J. P. Schlegel and C. B. Harris, Determining Transition-State Geometries in Liquids Using 2D-IR, *Science*, 2008, **319**, 1820–1823.

63 L. Chuntonov, Using Mirrors to Control Molecular Dynamics, *Science*, 2022, **378**, 712.

64 R. Yin and B. Jiang, Mechanical Vibrational Relaxation of NO Scattering from Metal and Insulator Surfaces: When and Why They Are Different, *Phys. Rev. Lett.*, 2021, **126**, 156101.

65 H. Bian, J. Li, X. Wen and J. Zheng, Mode-Specific Intermolecular Vibrational Energy Transfer. I. Phenyl Selenocyanate and Deuterated Chloroform Mixture, *J. Chem. Phys.*, 2010, **132**, 184505.

66 Y. R. Shen, *The Principles of Nonlinear Optics*, Wiley-Interscience, New York, United States, 1984.

67 I. Morichika, K. Murata, A. Sakurai, K. Ishii and S. Ashihara, Molecular Ground-State Dissociation in the Condensed Phase Employing Plasmonic Field Enhancement of Chirped Mid-Infrared Pulses, *Nat. Commun.*, 2019, **10**, 3893.

68 J. P. Kraack and P. Hamm, Vibrational Ladder-Climbing in Surface-Enhanced, Ultrafast Infrared Spectroscopy, *Phys. Chem. Chem. Phys.*, 2016, **18**, 16088–16093.

69 C. L. Anfuso, A. M. Ricks, W. Rodríguez-Córdoba and T. Lian, Ultrafast Vibrational Relaxation Dynamics of a Rhenium Bipyridyl CO_2-Reduction Catalyst at a Au Electrode Surface Probed by Time-Resolved Vibrational Sum Frequency Generation Spectroscopy, *J. Phys. Chem. C*, 2012, **116**, 26377–26384.

70 A. Ge, B. Rudshteyn, J. Zhu, R. J. Maurer, V. S. Batista and T. Lian, Electron-Hole-Pair-Induced Vibrational Energy Relaxation of Rhenium Catalysts on Gold Surfaces, *J. Phys. Chem. Lett.*, 2018, **9**, 406–412.

71 N. S. Mueller, R. Arul, L. A. Jakob, M. O. Blunt, T. Földes, E. Rosta and J. J. Baumberg, Collective Mid-Infrared Vibrations in Surface-Enhanced Raman Scattering, *Nano Lett.*, 2022, **22**, 7254–7260.

72 Z. Yu and R. R. Frontiera, Intermolecular Forces Dictate Vibrational Energy Transfer in Plasmonic-Molecule Systems, *ACS Nano*, 2022, **16**, 847–854.

73 S. A. Dönges, R. P. Cline, S. E. Zeltmann, J. Nishida, B. Metzger, A. M. Minor, J. D. Eaves and M. B. Raschke, Multidimensional Nano-Imaging of Structure, Coupling, and Disorder in Molecular Materials, *Nano Lett.*, 2021, **21**, 6463–6470.

74 J. F. Li, X. D. Tian, S. B. Li, J. R. Anema, Z. L. Yang, Y. Ding, Y. F. Wu, Y. M. Zeng, Q. Z. Chen, B. Ren, Z. L. Wang and Z. Q. Tian, Surface Analysis Using Shell-Isolated Nanoparticle-Enhanced Raman Spectroscopy, *Nat. Protoc.*, 2013, **8**, 52–65.

75 H. Y. Jung, Y. K. Park, S. Park and S. K. Kim, Surface Enhanced Raman Scattering from Layered Assemblies of Close-Packed Gold Nanoparticles, *Anal. Chim. Acta*, 2007, **602**, 236–243.

76 Y. K. Park and S. Park, Directing Close-Packing of Midnanosized Gold Nanoparticles at a Water/Hexane Interface, *Chem. Mater.*, 2008, **20**, 2388–2393.

77 Q. B. Pei, X. X. Zheng, J. J. Tan, Y. Luo and S. J. Ye, Probing the Local Near-Field Intensity of Plasmonic Nanoparticles in the Mid-infrared Spectral Region, *J. Phys. Chem. Lett.*, 2024, **15**, 5390–5396.

78 X. X. Zheng, Q. B. Pei, J. J. Tan, S. Y. Bai, Y. Luo and S. J. Ye, Local Electric Field in Nanocavities Dictates the Vibrational Relaxation Dynamics of Interfacial Molecules, *Chem. Sci.*, 2024, **15**, 11507–11514.

79 J. J. Tan, Z. J. Ni and S. J. Ye, Protein-Water Coupling Tunes the Anharmonicity of Amide I Modes in the Interfacial Membrane-Bound Proteins, *J. Chem. Phys.*, 2022, **156**, 105103.